On the synthesis and design of a novel backdrivable high-stiffness capstan drive

Jordan M. Longval and Clément Gosselin
Département de génie mécanique
Université Laval
1065 Avenue de la Médecine
Québec, Qc G1V0A6
Canada
Jordan.Longval.1@ulaval.ca, Clement.Gosselin@gmc.ulaval.ca

ABSTRACT

This article introduces a novel backdrivable high-stiffness cable capstan drive architecture for robotics applications. The drive has a low transmission ratio and a higher stiffness than typical capstan drives. The higher transmission stiffness is obtained by the use of grooves on both the input and the output pulleys of the drive which increases the effective coefficient of friction between the pulleys and the cable. The groove on the input pulley forms a single helix while the grooves on the output pulley form a R-helix, where R is equal to the transmission ratio of the drive. This property enables several different multi-cable arrangements for the drive, which further increases the transmission stiffness. A kinematic model of the capstan drive is established and used to ensure the proper alignment of the input pulley groove and output pulley grooves as a function of the distance between the pulleys. A 3D printed prototype of the transmission is presented.

1 Introduction

Robotic manipulators typically use transmissions with large reduction ratios in order to reduce the size and mass of the actuators. Such transmissions (e.g. harmonic drives) are not backdrivable, which is a limitation in some applications. For example, in Collaborative Robots (CR), it is desired to provide physical Human-Robot Interaction (pHRI), i.e., to allow users to manipulate the robot links directly.

Because their transmissions are not backdrivable, most CR used nowadays require force sensors to enable task teaching through pHRI. The force sensors are either placed near the CR's end effector [1] [2] [3] or inside each joint of the CR through the use of strain gauges [4]. The use of force/torque sensors limits the bandwidth of the pHRI and makes the interaction less intuitive and agile.

It is possible to teach CR tasks through pHRI without using force sensors. To this end, alternative robot kinematic architectures coupled with backdrivable Low-Ratio Transmissions (LRT) can be used. Alternative robot kinematic architectures can be used to move the CR actuators toward the base in order to minimize the influence of their inertia on the robot dynamics and payload capabilities while allowing larger and stronger actuators with backdrivable transmissions. This concept is already used in industrial palletizing robots [5], haptic devices [6] and backdrivable pHRI robots [7] [8].

LRT are already used in haptic devices for telesurgery [9] [10] [11] [12]. Yet, not all LRT are mechanically backdrivable. For example, a worm gear cannot be driven by its output (through the worm).Table 1 shows a list of backdrivable LRT and indicates their advantages and disadvantages for pHRI.

Table 1 shows that a capstan drive is a good choice of backdrivable LRT because it has higher stiffness than a belt drive and it has a low backlash like gears or chain drives. This is why it is used in haptic devices [10] [13], highly backdrivable collaborative robots [14] [15] [16] and high precision targeting systems [17] [18] [19] [20]. Having low backlash is very important for robotics applications which require the robot's motors to work in both directions at a high frequency [21] [22]. However, Table 1 also shows that capstan drives have lower stiffness than other LRT such as gears and can be subject to slip error [19] [23].

Table 1: Comparison of different backdrivable LRT.

LRT type	Advantages	Disadvantages
Spur and helical gears	High stiffness High torque capability	Clearance between teeth (backlash)
Belt drive	Transmission over a larger distance No backlash	Lower stiffness Slip error
Chain Drive	High stiffness	Clearance between inner links Higher transmission inertia
Cable (capstan drive)	Higher stiffness than belt drive No backlash	Lower stiffness than chain and gears Slip error

In order to alleviate these drawbacks, this article presents a novel capstan architecture that increases the stiffness of the transmission by using grooves on the transmission's pulleys. The grooves increase the friction coefficient between the cable and the pulleys, which makes the transmission stiffer. This concept has already been used in cable transmissions for elevators as described in [24] and [25] Moreover, the novel capstan drive allows multiple cable arrangements, which further increases the stiffness of the transmission.

This paper is structured as follows. In Section 2 and 3, the general modelling of a capstan drive and its torsional stiffness are recalled. The theoretical model used here is based on the work of Werkmeister et al. [26]. Part of this model is also used in [23]. Section 4 discusses the fact that grooves etched along the surface of a capstan drive's pulleys can theoretically increase the friction coefficient between the drive's cable and its pulleys thus increasing the overall stiffness of the capstan drive. This effect has been discussed in different reference books such as [24] and [25]. The result of an experiment which proves this effect is also presented in section 4. The use of grooves in capstan drives has already been presented in [18]. However, this paper presents a novel design for the output pulley of a capstan drive which uses grooves arranged as a multiple helix. The novel design enables different multi-cable arrangements of the capstan drive that can theoretically further increase its torsional stiffness. The novel capstan drive architecture as well as different possible cable arrangements are presented in Section 5. The advantages and disadvantages of each of the proposed arrangements are discussed. Section 6 then proposes a method to properly arrange the capstan drive's pulleys during the drive's assembly so that the cables can follow a smooth and continuous path while passing from one pulley to the other while avoiding cable interference. Section 7 shows that it is always possible to avoid two cables interfering with one another if the distance between the pulleys is large enough. Finally, concluding remarks are made in Section 9.

2 Modelling of a capstan drive

Figure 1 presents the different elements of the capstan drive model. In figure 1, r_1 is the radius of the small input pulley while r_2 is the radius of the large output pulley. The transmission ratio is given by $R = \frac{r_2}{r_1}$. The cable passes from the large pulley to the small pulley and back to the large pulley in a lemniscate shaped pattern indicated by the red arrows in figure 1. A preload tension T_p is applied on the cable by pulling on the cable with a mechanism alike a turnbuckle (at point P_1) and by fixing the other end of the cable to the pulley(at point P_2).

When a torque τ_i is applied on the input pulley, one side of the cable extends while the other part of the cable shortens. The extension is caused by an increase in the tension in the cable by an amount T_ℓ while the contraction
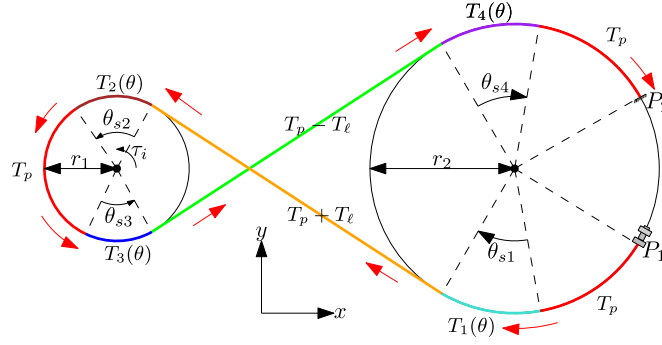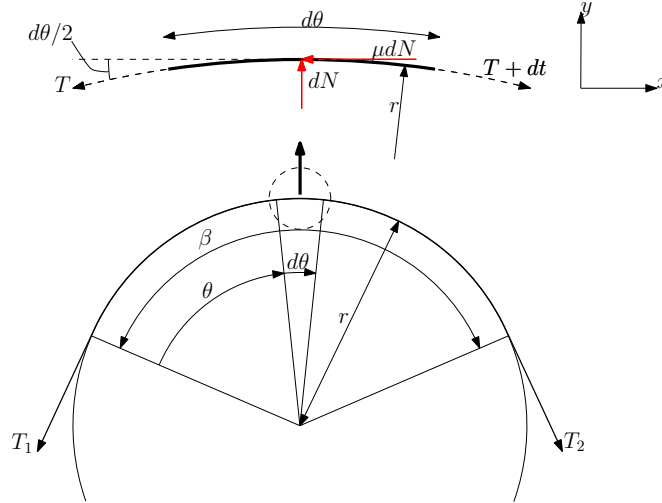
Fig. 1: Modelling of a capstan drive.

Fig. 2: Small segment of the cable pulley interaction.

of the other part of the cable is caused by a reduction of the tension by an equal amount T_ℓ. The tension on the taught side becomes $T_p + T_\ell$ while the tension on the loose side becomes $T_p - T_\ell$. The torque balance equation about the axis of rotation of the input pulley can be written as

$$\tau_i - (T_p + T_\ell)r_1 + (T_p - T_\ell)r_1 = 0, \tag{1}$$

which yields

$$T_\ell = \frac{\tau_i}{2r_1}. \tag{2}$$

The tension variations in the cable occur in contact regions between the cable and the pulleys called the slip regions. These regions are represented in figure 1 with the angles θ_{s1} to θ_{s4}. Along these slip regions, the cable elongates or shortens due to the applied torque. This local variation in length causes friction between the pulleys and the cable. Figure 2 illustrates this principle.

Figure 2 shows a small segment of a cable lying on the surface of a pulley of radius r. The small cable segment is lying on a small angle segment of the pulley $d\theta$. The static friction coefficient between the pulley and the cable is μ. The tension on one end of the small cable segment is T while it is $T + dT$ at the other end. The small tension variation is created by an applied torque on the pulley. The normal force between the small cable segment and the pulley is dN. When torque is applied to the pulley, the pulley surface creates a friction force on the cable segment of μdN in the tangential direction of the torque. Calculating the force balance on the cable

segment gives

$$\sum F_x = T\cos\left(\frac{d\theta}{2}\right) - (T+dT)\cos\left(\frac{d\theta}{2}\right) + \mu dN = 0, \tag{3}$$

$$\sum F_y = -T\sin\left(\frac{d\theta}{2}\right) - (T+dT)\sin\left(\frac{d\theta}{2}\right) + dN = 0. \tag{4}$$

Since $d\theta$ is a small angle and dT is a small tension variation, the following approximations can be made

$$\sin\left(\frac{d\theta}{2}\right) \approx \frac{d\theta}{2}, \quad \cos\left(\frac{d\theta}{2}\right) \approx 1, \quad dT d\theta \approx 0. \tag{5}$$

Applying these approximations to(3) and (4) gives

$$\frac{dT}{T} = \mu d\theta. \tag{6}$$

In figure 2, when the tension varies from T_1 to T_2 where $T_2 > T_1$, the integration over the angle β of (6) gives

$$\beta = \frac{1}{\mu}\ln\left(\frac{T_2}{T_1}\right). \tag{7}$$

Angle β is referred to as the slip angle of the slip region. Integrating from T_1 to a function $T(\theta)$ over the slip region then gives

$$T(\theta) = T_1 e^{\mu\theta}, \quad 0 < \theta < \beta. \tag{8}$$

The same can be said by integrating from the max tension T_2 to a smaller tension $T(\theta)$ over the slip region β, which gives

$$T(\theta) = T_2 e^{-\mu\theta}, \quad 0 < \theta < \beta. \tag{9}$$

Applying (7), (8) and (9) to the slip regions in figure 1, one finds

$$T_1(\theta) = T_p e^{\mu\theta}, \quad 0 < \theta < \theta_{s1}, \quad \theta_{s1} = \frac{1}{\mu}\ln\left(\frac{T_p + T_\ell}{T_p}\right), \tag{10}$$

$$T_2(\theta) = (T_p + T_\ell)e^{-\mu\theta}, \quad 0 < \theta < \theta_{s2}, \quad \theta_{s2} = \theta_{s1}, \tag{11}$$

$$T_3(\theta) = T_p e^{-\mu\theta}, \quad 0 < \theta < \theta_{s3}, \quad \theta_{s3} = \frac{1}{\mu}\ln\left(\frac{T_p}{T_p - T_\ell}\right), \tag{12}$$

$$T_4(\theta) = (T_p - T_\ell)e^{\mu\theta}, \quad 0 < \theta < \theta_{s4}, \quad \theta_{s4} = \theta_{s3}. \tag{13}$$

Equations (10) to (13) describe the variation of the tension along the cable. These equations are used in the following section to model the stiffness of a capstan drive.

3   Stiffness model of a capstan drive

Hooke's law gives the relationship between the tensile force in an elastic object and its strain. The strain of an elastic object is also defined as its variation in length over its original length. Expressing this definition of strain

in an infinitesimal form and equating it to Hooke's law, one can then write

$$\varepsilon \equiv \frac{d\delta}{dL} = \frac{F}{AE}, \Rightarrow d\delta = \frac{FdL}{AE} \tag{14}$$

where ε is the strain, $d\delta$ is a very small length variation, dL is a very small cable length, F is the tensile force applied on the elastic object, A is the object's cross section area and E is its Young modulus. Equation (14) can be integrated to determine the cable deformation.

The cable deformation δ_i along the slip region θ_{si} is equal to the total deformation along the slip region minus the initial deformation caused by the preload. Using (14) and using the fact that $dL = rd\theta$, the deformations δ_i are obtained as

$$\delta_i = \frac{r}{AE} \left(\int_0^{\theta_{si}} T_i(\theta)d\theta - T_p \int_0^{\theta_{si}} d\theta \right), \quad i = 1,\ldots,4 \tag{15}$$

where $r = r_2$ for θ_{s1} and θ_{s4} and $r = r_1$ for θ_{s2} and θ_{s3}. Applying (15) to the slip angle θ_{s1} gives

$$\delta_1 = \frac{T_p r_2}{AE} \left(\int_0^{\theta_{s1}} e^{\mu\theta}d\theta - \int_0^{\theta_{s1}} d\theta \right), \tag{16}$$

$$= \frac{T_p r_2}{AE} \left(\frac{1}{\mu} \left(e^{\mu\theta_{s1}} - 1 \right) - \theta_{s1} \right), \tag{17}$$

$$= \frac{r_2}{\mu AE} \left(T_\ell - T_p \ln \left(\frac{T_p + T_\ell}{T_p} \right) \right). \tag{18}$$

Similarly for δ_2 to δ_4, one obtains

$$\delta_2 = \frac{r_1}{\mu AE} \left(T_\ell - T_p \ln \left(\frac{T_p + T_\ell}{T_p} \right) \right), \tag{19}$$

$$\delta_3 = \frac{r_1}{\mu AE} \left(T_\ell - T_p \ln \left(\frac{T_p}{T_p - T_\ell} \right) \right), \tag{20}$$

$$\delta_4 = \frac{r_2}{\mu AE} \left(T_\ell - T_p \ln \left(\frac{T_p}{T_p - T_\ell} \right) \right). \tag{21}$$

Some cable deformation also occurs in the cable sections which are not in contact with the pulleys. These cable sections are here called the free sections and the deformation along these sections is obtained by integrating (14) which gives

$$\delta_{f1} = \frac{T_p + T_\ell}{AE} \int_0^{L_f} dL = \frac{T_p + T_\ell}{AE} L_f, \tag{22}$$

$$\delta_{f2} = \frac{T_p - T_\ell}{AE} \int_0^{L_f} dL = \frac{T_p - T_\ell}{AE} L_f, \tag{23}$$

where δ_{f1} and δ_{f2} are the deformations on the tight and slack side respectively and L_f is the length of the free parts of the cable which are not in contact with the pulleys.

The compliance of the different cable sections can be defined as the absolute value of the variation in deformation of the cable as a function of the applied load. Mathematically, this means that the compliance of the different cable sections can be obtained by differentiating the deformation expressions in (18) to (23) with respect to T_ℓ. Furthermore, since compliance is the inverse of stiffness, one can easily obtain the stiffness of the different

cable sections. For the slip regions, this gives

$$C_{si} = \left| \frac{d\delta_{si}}{dT_\ell} \right|, \quad i = 1, \ldots, 4, \tag{24}$$

$$\Rightarrow C_{s1} = \frac{r_2}{AE\mu} \left(\frac{T_\ell}{T_p + T_\ell} \right) = \frac{1}{K_{s1}} \tag{25}$$

$$\Rightarrow C_{s2} = \frac{r_1}{AE\mu} \left(\frac{T_\ell}{T_p + T_\ell} \right) = \frac{1}{K_{s2}} \tag{26}$$

$$\Rightarrow C_{s3} = \frac{r_1}{AE\mu} \left(\frac{T_\ell}{T_p - T_\ell} \right) = \frac{1}{K_{s3}} \tag{27}$$

$$\Rightarrow C_{s4} = \frac{r_2}{AE\mu} \left(\frac{T_\ell}{T_p - T_\ell} \right) = \frac{1}{K_{s1}} \tag{28}$$

For the stiffnesses of the free sections of the cable, one obtains

$$K_{f1} = K_{f2} = \frac{AE}{L_f} \tag{29}$$

The total stiffness of the capstan transmission is obtained by combining the individual stiffnesses of the cable segments along the transmission. The stiffness elements K_{s1}, K_{f_1} and K_{s2} form a serial combination of springs. The same can be said for K_{s3}, K_{f_2} and K_{s4}. The two serial springs groups are in parallel to one another meaning that the total stiffness of the transmission can be written as

$$K = K_1 + K_2, \tag{30}$$

where

$$K_1 = \frac{1}{\frac{1}{K_{s1}} + \frac{1}{K_{f1}} + \frac{1}{K_{s2}}}, \tag{31}$$

$$K_2 = \frac{1}{\frac{1}{K_{s3}} + \frac{1}{K_{f2}} + \frac{1}{K_{s4}}}. \tag{32}$$

The total stiffness K represents the linear stiffness of the transmission. Since a capstan drive is a torsional element, a better indicator of its stiffness is the drive's torsional stiffness when one of its pulleys is held rigidly. The torsional stiffness K_t of the capstan drive when the small pulley is held rigidly and a torque τ is applied on the large pulley, causing an angular displacement α, is then given by

$$\tau = K_t \alpha. \tag{33}$$

The relationship between K_t and K is obtained by writing

$$\frac{\tau_D}{r_2} = K\delta \tag{34}$$

$$\alpha = \frac{\delta}{r_2}. \tag{35}$$

Equation (34) gives the relationship between a torque τ applied on the large pulley of radius r_2 and the total linear displacement δ when the small pulley is held tightly. Equation (35) gives the relationship between the total linear displacement of the cable and the angular displacement α of the large pulley of radius r_2. Using these two
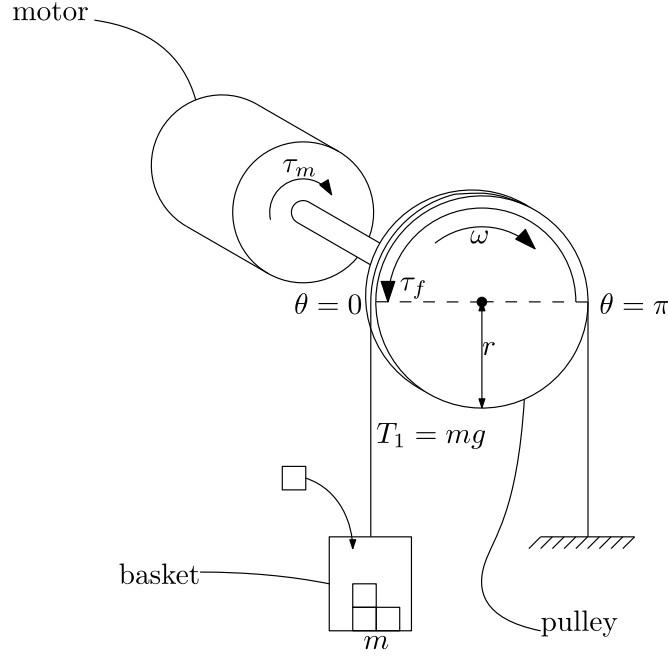
Fig. 3: Explicative illustration of the experimental setup.

equations with (33) yields

$$K_t = K r_2^2. \tag{36}$$

The following section shows how placing the capstan transmission's cable into grooves helps to increase the coefficient of friction between the cable and the pulleys and therefore the transmission's stiffness.

4 Influence of grooves on the capstan drive stiffness

Analyzing the equations for the stiffness of the different cable sections of a capstan drive ((24) to (28)), one can clearly see that most of the stiffness terms are proportional to the coefficient of friction. Therefore, Increasing the coefficient of friction between the cable and the pulleys is an effective way to increase the overall stiffness of the transmission. Typically, the coefficient of friction is a property that is only dependant on the nature of the materials at the friction interface. However, like for a v-belt drive, by changing the geometry of the interface between two surfaces, it is possible to change the apparent coefficient of friction. The way a circular groove interacts with a cable to increase the apparent coefficient of friction has been studied many times as grooves are often used in elevator mechanical design [24] [25] [27] [28]. According to the afformentioned references, the apparent coefficient of friction μ' for a circular groove is written as

$$\mu' = \frac{4}{\pi}\mu, \tag{37}$$

where μ is the static coefficient of friction between the cable and a flat surface of the same material as the groove. This means that the use of grooves theoretically increases the friction between the cable and the groove by roughly 27.3 %.

To prove this concept, a small experimental setup was made. The experimental setup is shown in figures 3 and **??**. In this setup, a pulley is connected to a motor which is controlled to spin at a constant speed. a rope is passed around the top half of the pulley with one end of the rope attached to a very heavy mass (immovable) and the other end of the rope attached to a basket. The cable slips on the pulley as the number of turns around the pulley (1/2) is insufficient to create traction. As more and more mass is added to the basket, the friction between the cable and the pulley increases. Therefore, a larger torque τ_m is required at the motor in order to maintain a constant speed. When the motor spins at constant speed, the torque required is equal to the total friction torque

7
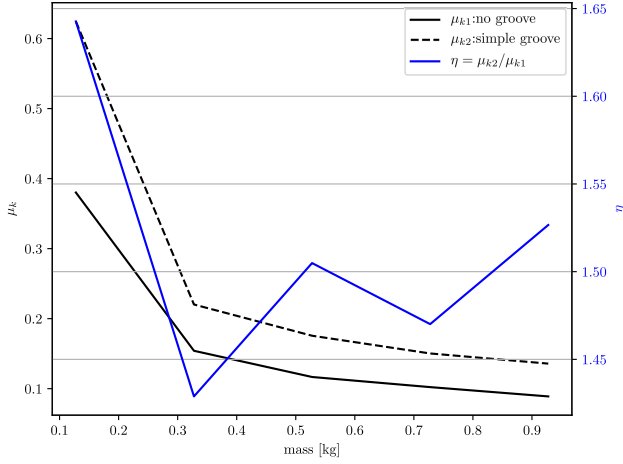
Mass [g]	μ_{k1}:no groove	μ_{k2}:simple	$\eta = \mu_{k2}/\mu_{k1}$
127.6	0.38	0.62	1.64
327.6	0.15	0.22	1.43
527.6	0.12	0.18	1.50
727.6	0.10	0.15	1.47
927.6	0.09	0.13	1.53

Fig. 4 & Table 2: Experimental results.

(if the internal friction torque of the motor is neglected). The total friction torque τ_f, for this setup, is written as

$$\tau_f = r\mu \int_0^\pi dN(\theta), \tag{38}$$

where r is the radius of the experimental pulley, μ is the friction coefficient, $dN(\theta)$ is the equivalent normal force between the cable and the pulley at the angle θ around the wrapping area. Using equations (4) and (9), the integration in equation (38) can be rewritten as

$$\tau_f = r\mu \int_0^\pi dN(\theta) = r\mu T_1 \int_0^\pi e^{-\mu\theta} d\theta = r\mu mg \int_0^\pi e^{-\mu\theta} d\theta = rmg\left(1 - e^{\mu\pi}\right). \tag{39}$$

In order to have constant speed, one must have $\tau_f = \tau_m$ which means that μ can be calculated as a function of the mass of the basket m and the motor torque τ_m with the following equation

$$\mu = \frac{1}{\pi} \ln\left(\frac{rmg}{rmg - \tau_m}\right). \tag{40}$$

In the experimental setup, two pulleys of radius $r = 0.03$ m were tested, one with no groove and one with a groove of same radius as the cable in order to have a full half circled groove. The motor was spun at a constant speed of 100 RPM while the motor torque was recorded continously. The mass of the basket was increased incrementally from 100 g of added mass to 900 grams of added mass (the basket having a mass of 27.6 g). The average motor torque for every mass increment was also recorded. The experiment results are presented in Table 2 and in figure 4.

As can be seen in the experimental results, the increase in the coefficient of friction when passing from no groove to a simple half circle groove is even more than what the theory predicts as the average increase is of 1.51 times the no groove coefficient of friction. This shows that the use of grooves is indeed a good way to easily increase the coefficient of friction between the cables and the pulleys and thus increase the total stiffness of a capstan drive.

The following section presents a novel capstan drive architecture that takes advantage of the increased effective friction coefficient of grooved pulleys and uses multiple grooves on its output pulley in order to allow different cable arrangements which further increase the stiffness of the drive.
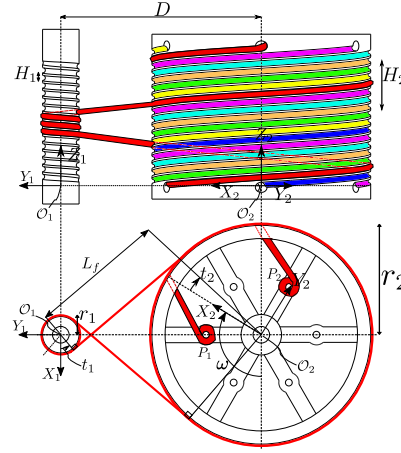
Fig. 5: Architecture of the novel capstan drive.

5 Novel capstan drive architecture

The novel architecture is presented in figure 5. The novel capstan drive is composed of two pulleys, the input pulley of radius r_1 which is connected to the motor and the output pulley of radius r_2 which is connected to the output of the drive. A cable indicated by a red line goes from the output pulley to the input pulley and back to the output pulley. Points P_1 and P_2 are anchoring points where the cable is fixed. The grooves on each pulley have identical cross sections. However, the groove on the input pulley forms a single helix with a pitch of H_1 while the grooves on the output pulley form a R-helix where R is the reduction ratio of the drive, i.e. r_2/r_1. In figure 5, the grooves on the output pulley are each indicated with a different colour to help differentiate them. Each of the output grooves has a pitch of H_2, where $H_2 = RH_1$. The grooves of the output pulley evolve in a direction opposite that of the grooves of the input pulley. The free cable length L_f indicates the part of the cable that is not in direct contact with either of the drive pulleys. The distance between the centre axes of the pulleys is noted D.

The presence of grooves on both the input and the output pulleys helps to increase the stiffness of the drive by increasing the effective coefficient of friction between the cable and the pulleys, as mentioned in the preceding section. Furthermore, the multiple grooves present on the output pulley enable the use of multiple cables in different cable arrangements, which can further increase the stiffness of the drive.

Figure 6 illustrates the different possible cable arrangements. In figure 6a, a single cable is used which is fixed at both ends to the output pulley. This arrangement has the advantage of being simple and its stiffness model is equivalent to the stiffness model of a typical capstan drive such as the one presented in figure 1. This arrangement can be used many times in parallel as shown in figure 6b in order to multiply the total stiffness of the transmission. However, since none of the cables are fixed to the input pulley, slipping of the input pulley is possible.

The layout shown in figure 6c uses two cables. Each cable is fixed to the input pulley at one end and to the output pulley at the other end. This cable arrangement has the advantage of ensuring that the input pulley does not slip. However, it requires two cables to obtain a transmission stiffness which is equivalent to the transmission stiffness of a single cable arrangement in figure 6a.

The layout shown in figure 6d uses three cables. Two of its cables are fixed to both the input and output pulley while its third cable is strictly fixed to the output pulley but loops over the input pulley. The first two cables ensure the motion coupling of the input and output pulley (that there is no slipping) while the third cable helps to increase the transmission stiffness. This cable arrangement has the advantages of the two previous arrangements.

In all the cable arrangements shown in figure 6, the number of turns that can be made by the output pulley is given by

$$N = \frac{d-a}{H_1 R},$$

(41)

where d and a are defined in figure 6, H_1 is the pitch of the groove on the input pulley and R is the reduction ratio of the drive. In order for the cables to pass from the input pulley to the output pulley and vice versa, geometric conditions must be met in order to ensure that the helical path described by the input groove aligns with one of the helical paths of the output pulley grooves. The following section presents a mathematical model that ensures proper alignment.
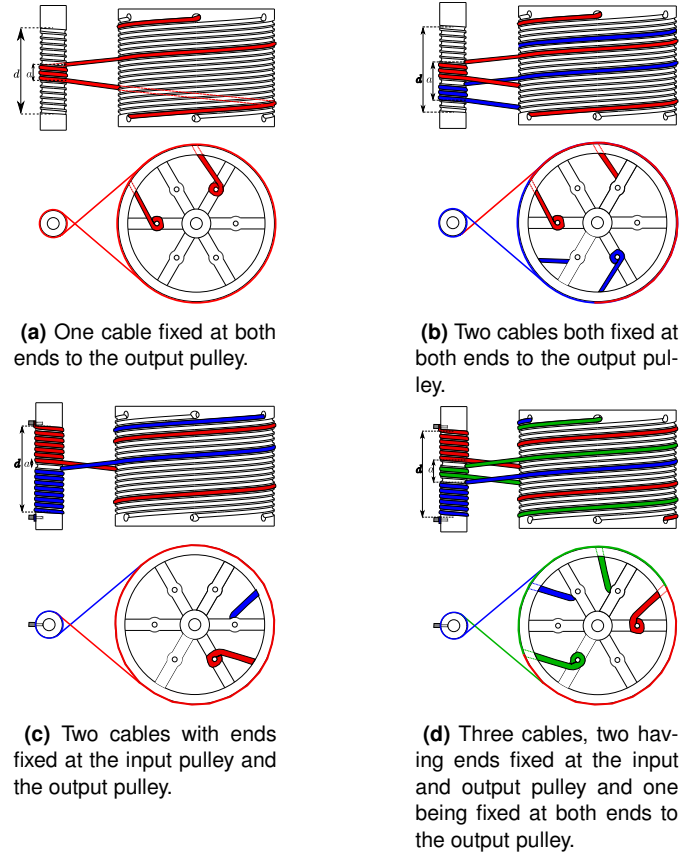
(a) One cable fixed at both ends to the output pulley.

(b) Two cables both fixed at both ends to the output pulley.

(c) Two cables with ends fixed at the input pulley and the output pulley.

(d) Three cables, two having ends fixed at the input and output pulley and one being fixed at both ends to the output pulley.

Fig. 6: Different possible cable arrangements.

6   Alignment of the input and output grooves

The groove on the input pulley can best be described as a helix. The parametric helix function of the groove on the input pulley is given by

$$\mathbf{p}_1(t_1) = \begin{bmatrix} r_1 \cos t_1 \\ -r_1 \sin t_1 \\ \frac{H_1 t_1}{2\pi} \end{bmatrix} \tag{42}$$

with respect to the reference frame of the input pulley O_1. The X_1 axis of O_1 points towards the starting point of the helix. In (42), t_1 is the helix parameter of the trajectory. The second term of $\mathbf{p}_1(t_1)$ has a negative sign since the helix on the input pulley evolves in a direction opposite to the reference frame O_1. Differentiating $\mathbf{p}_1(t_1)$ with respect to t_1 gives a vector that is tangent to $\mathbf{p}_1(t_1)$ and which can be written as

$$\mathbf{q}_1(t_1) = \frac{d\mathbf{p}_1(t_1)}{dt_1} = \begin{bmatrix} -r_1 \sin t_1 \\ -r_1 \cos t_1 \\ \frac{H_1}{2\pi} \end{bmatrix} \tag{43}$$

The unit vector $\mathbf{u}_1(t_1)$ along $\mathbf{q}_1(t_1)$ is obtained by dividing $\mathbf{q}_1(t_1)$ by its Euclidean norm which gives

$$\mathbf{u}_1(t_1) = \frac{\mathbf{q}_1(t_1)}{\rho_1}, \quad \rho_1 = \frac{\sqrt{H_1^2 + 4\pi^2 r_1^2}}{2\pi}. \tag{44}$$

The grooves on the output pulley can also be described by parametric helix functions. These functions can be written as

$$\mathbf{p}_{2i}(t_{2i}) = \begin{bmatrix} r_2 \cos t_{2i} \\ r_2 \sin t_{2i} \\ \frac{H_2 t_{2i}}{2\pi} \end{bmatrix}, \tag{45}$$

$$t_{2i} = t_2 + \frac{(i-1)}{R} 2\pi, \quad i = 1, \ldots, R, \tag{46}$$

with respect to the reference frame of the output pulley O_2. The X_2 axis points towards the starting point of one of the output grooves. In (46), t_2 is the general helix parameter of the output pulley and the t_{2i} parameters are specific to each individual groove of the output pulley.

Differentiating vectors $\mathbf{p}_{2i}(t_{2i})$ with respect to t_2 gives vectors that are tangent to their respective $\mathbf{p}_{2i}(t_{2i})$ vectors. These tangent vectors can be written as

$$\mathbf{q}_{2i}(t_{2i}) = \frac{d\mathbf{p}_{2i}(t_{2i})}{dt_2} = \begin{bmatrix} -r_2 \sin t_{2i} \\ r_2 \cos t_{2i} \\ \frac{H_2}{2\pi} \end{bmatrix}, \quad i = 1, \ldots, R. \tag{47}$$

The tangent unit vectors along the $\mathbf{q}_{2i}(t_{2i})$ vectors are given by

$$\mathbf{u}_{2i}(t_{2i}) = \frac{\mathbf{q}_{2i}}{\rho_2}, \quad \rho_2 = \frac{\sqrt{H_2^2 + 4\pi^2 r_2^2}}{2\pi}, \quad i = 1, \ldots, R. \tag{48}$$

The helix functions of the input pulley groove and one of the output pulley grooves can be expressed as a function of one another in the following loop closure equation

$$\mathbf{p}_1 + L_f \mathbf{u}_1 = \mathbf{a} + \mathbf{Q} \mathbf{p}_{2i}, \quad i = 1, \ldots, R, \tag{49}$$

where $\mathbf{a} = \begin{bmatrix} 0 & -D & 0 \end{bmatrix}^T$ is a vector expressed in the O_1 reference frame and $\mathbf{Q}$ is a rotation matrix expressing a change of reference frame from O_2 to O_1 and is written as

$$\mathbf{Q} = \begin{bmatrix} \cos \omega & -\sin \omega & 0 \\ \sin \omega & \cos \omega & 0 \\ 0 & 0 & 1 \end{bmatrix}, \tag{50}$$

where ω represents the amount of rotation of the output pulley needed in order to have the cables pass smoothly between the two pulleys. Equation (49) is equivalent to the three following scalar equations

$$r_1 \left(\cos t_1 - \frac{L_f}{\rho_1} \sin t_1 \right) = r_2 \cos(\omega + t_{2i}), \tag{51}$$
$$i = 1, \ldots, R,$$

$$-r_1 \left(\sin t_1 + \frac{L_f}{\rho_1} \cos t_1 \right) = -D + r_2 \sin(\omega + t_{2i}), \tag{52}$$
$$i = 1, \ldots, R,$$

$$H_1\left(t_1 + \frac{L_f}{\rho_1}\right) = H_2 t_2. \tag{53}$$

In addition to these equations, in order to ensure the proper alignment of the input and output pulley grooves, one must be able to draw a straight line from the input groove to one of the output grooves where the line is tangent to both grooves. This can be mathematically written as

$$\mathbf{q}_1 \times \mathbf{Q}\mathbf{q}_{2i} = \mathbf{0}, \ \ i = 1, \ldots, R, \tag{54}$$

which is equivalent to the following three scalar equations

$$\frac{H_2 r_1}{2\pi}\cos t_1 + \frac{H_1 r_2}{2\pi}\cos(\omega + t_{2i}) = 0, \ \ i = 1, \ldots, R, \tag{55}$$

$$\frac{H_2 r_1}{2\pi}\sin t_1 - \frac{H_1 r_2}{2\pi}\sin(\omega + t_{2i}) = 0, \ \ i = 1, \ldots, R, \tag{56}$$

$$\sin\left(t_1 + t_{2i} + \omega\right) = 0, \ \ i = 1, \ldots, R. \tag{57}$$

From (57), we obtain that

$$t_1 + t_{2i} + \omega = n\pi, n \in \mathbb{N}, \ \ i = 1, \ldots, R. \tag{58}$$

Substituting (58) into (55) and (56) yields

$$\frac{H_2 r_1}{2\pi}\cos t_1 + \frac{H_1 r_2}{2\pi}\cos(n\pi - t_1) = 0, \ \ i = 1, \ldots, R, \tag{59}$$

$$\frac{H_2 r_1}{2\pi}\sin t_1 - \frac{H_1 r_2}{2\pi}\sin(n\pi - t_1) = 0, \ \ i = 1, \ldots, R. \tag{60}$$

Equations (59) and (60) are both satisfied if

$$H_2 r_1 = H_1 r_2 \tag{61}$$

and

$$n = 2m + 1, \ \ m \in \mathbb{N}. \tag{62}$$

Equations (58), (61) and (62) represent the conditions that must be met in order to be able to draw a straight line from the input pulley groove to one of the output pulley grooves where the line is tangent to both grooves. Substituting these conditions into (51) and (53) leads to

$$(r_2 + r_1)\cos t_1 = \frac{L_f r_1}{\rho_1}\sin t_1, \tag{63}$$

$$D - (r_2 + r_1)\sin t_1 = \frac{L_f r_1}{\rho_1}\cos t_1. \tag{64}$$

Dividing (63) by (64) and rearranging then yields

$$\sin t_1 = \left(\frac{r_2 + r_1}{D}\right). \tag{65}$$

The right-hand side term in (65) is bound between 0 and 1 since $D \in [(r_2 + r_1), \infty[$. This means that

$$t_1 = \varphi + 2\pi p, \quad p \in \mathbb{N} \tag{66}$$

or

$$t_1 = (2p+1)\pi - \varphi, \quad p \in \mathbb{N}, \tag{67}$$

$$\varphi = \sin^{-1}\left(\frac{r_1 + r_2}{D}\right). \tag{68}$$

Substituting (67) into (63), one finds that L_f would need to have a negative length, which is impossible. This is not the case when t_1 is given by (66) and therefore this is the only possible value for t_1. The value of L_f is thus

$$L_f = \frac{\rho_1}{r_1}\sqrt{D^2 - (r_2 + r_1)^2}. \tag{69}$$

Having L_f and t_1, one can finally find the value of ω using (53) and (58) as

$$\omega = (2m+1)\pi - t_1 - \frac{\left(t_1 + \frac{L_f}{\rho_1}\right)}{R} - \frac{2\pi(i-1)}{R}, \tag{70}$$
$$i = 1, \ldots, R, m \in \mathbb{N},$$

with t_1 given by (66) and L_f given by (69). Equation (70) can be simplified since the output pulley is $2\pi/R$ symmetric about the Z_2 axis in figure 5. The simplified version of (70) is written as

$$\omega = \left(\frac{-\left(\varphi(R+1) + \frac{L_f}{\rho_1}\right)}{R}\right) // \left(\frac{2\pi}{R}\right), \tag{71}$$

where $a//b$ returns the remainder of a divided by b.

Angle ω varies with the distance separating the axes of the input and output pulleys D. Knowing D, properly aligning the pulleys so that the cables follow a smooth path simply requires that both pulleys be locked during the cable mounting with the large pulley being rotated by an angle ω from the X_1 axis of the small pulley around the Z_2 axis of the large pulley. After having taught all the cables at both ends, the system can then be unlocked and the pulley grooves are properly aligned.

The following sections shows that their exists a minimal distance between the two capstan drive pulleys to ensure that their is no cable interference.

7 Minimal distance between pulleys to avoid cable interference.

The cable arrangements in figures 6c, 6b and 6d all display the situation where cable interference between two distinct cables might be possible if the distance between the pulleys is too small. However, one can determine the minimal distance D between the two capstan pulleys as a function of the cable diameter ζ. Figure 7 shows a modified version of figure 6c which includes a reference frame from which positions of interest can be established. In figure 7, points P_3 and P_4 are respectively the points where the blue and the red cable leave tangeantially the small pulley of radius r_3. The position of theses points with respect to the reference frame O_3 can be respectively
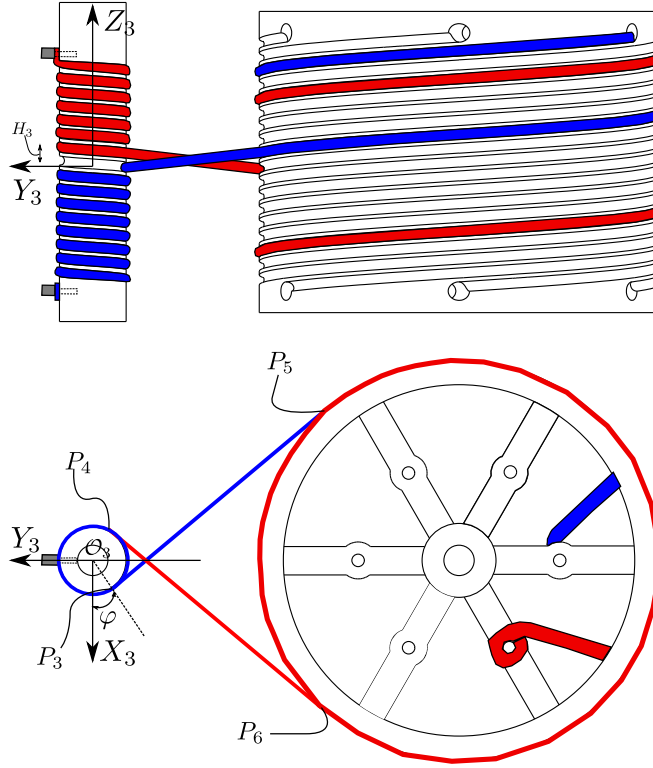
Fig. 7: Determining the shortest cable to cable distance in a two cable arrangement.

written as

$$P_3 : \mathbf{p}_3 = \begin{bmatrix} r_3 \cos\varphi \\ -r_3 \sin\varphi \\ \frac{H_3}{2\pi}\varphi \end{bmatrix}, \quad P_4 : \mathbf{p}_4 = \begin{bmatrix} -r_3 \cos\varphi \\ -r_3 \sin\varphi \\ \frac{H_3}{2\pi}(3\pi - \varphi) \end{bmatrix}, \tag{72}$$

where H_3 is the pitch of the input pulley helix and φ is given by

$$\varphi = \sin^{-1}\left(\frac{r_3 + r_4}{D}\right) \tag{73}$$

where r_3 is the radius of the small pulley, r_4 is the radius of the large pulley and D is the center to center distance between the two. Furthermore, the tangeant unit vectors at points P_3 and P_4 pointing in the direction leaving the small pulley can be expressed respectively as

$$\mathbf{u}_3 = \frac{\begin{bmatrix} -r_3 \sin\varphi \\ -r_3 \cos\varphi \\ \frac{H_3}{2\pi} \end{bmatrix}}{\rho_3}, \quad \mathbf{u}_4 = \frac{\begin{bmatrix} r_3 \sin\varphi \\ -r_3 \cos\varphi \\ \frac{-H_3}{2\pi} \end{bmatrix}}{\rho_3}, \quad \rho_3 = \frac{\sqrt{H_3^2 + 4\pi^2 r_3^2}}{2\pi}. \tag{74}$$

With vectors $\mathbf{p}_3$, $\mathbf{p}_4$, $\mathbf{u}_3$ and $\mathbf{u}_4$, one can describe two lines l_3 and l_4 which are coincident with the free blue and red cable segments in fig 7 and which are written parametrically as

$$l_3 : \mathbf{p}(s_3) = \mathbf{p}_3 + \mathbf{u}_3 s_3, \quad l_4 : \mathbf{p}(s_4) = \mathbf{p}_3 + \mathbf{u}_4 s_4, \quad s_3, s_4 \in \mathbb{R}, \tag{75}$$

14

where s_3 and s_4 are the parameters of the lines l_3 and l_4. It is well known that the smallest distance d between two skew lines l_A and l_B in respective parametric equations can be obtained as

$$l_A : \mathbf{p}(s_A) = \mathbf{m}_A s_A + \mathbf{b}_A, \quad l_B : \mathbf{p}(s_B) = \mathbf{m}_B s_A + \mathbf{b}_B, \quad \Rightarrow d = \left| \frac{\mathbf{m}_A \times \mathbf{m}_B}{\|\mathbf{m}_A \times \mathbf{m}_B\|} \cdot (\mathbf{b}_B - \mathbf{b}_A) \right|. \tag{76}$$

Applying this equation to the parametric lines l_3 and l_4 gives

$$d = \left| \frac{\mathbf{u}_3 \times \mathbf{u}_4}{\|\mathbf{u}_3 \times \mathbf{u}_4\|} \cdot (\mathbf{p}_4 - \mathbf{p}_3) \right| = \left| \frac{H_3(r_3 + r_4)(3\pi - 2\varphi) - 2\lambda}{\gamma} \right|, \tag{77}$$

where

$$\lambda = \sqrt{D^2 - (r_3 + r_4)^2} \tag{78}$$

and

$$\gamma = \sqrt{D^2 H_3^2 + 4\pi^2 r_3^2 (r_3 + r_4)^2}. \tag{79}$$

Finally, using equation (77) and replacing d by the diameter ζ, one can write the following condition which ensures that the cables will not touch

$$\left| \frac{H_3(r_3 + r_4)(3\pi - 2\varphi) - 2\lambda}{\gamma} \right| > \zeta. \tag{80}$$

Since the function in (77) increases with D and H_3, there will exist a couple D, H_3 which will satisfy the condition in (80) meaning it is always possible to avoid cable interference.

8 Multimedia extension

A video accompanies this paper. The video demonstrates the operation of a prototype of the novel capstan drive as well as its backdrivability.

9 Conclusion

This paper presented a novel capstan drive architecture which uses grooves on both its input and output pulleys in order to increase the effective coefficient of friction between the drive cables and the pulleys. Using a previously established model of a capstan drive, it was shown that increasing the coefficient of friction between the drive cables and the drive pulleys increases the drive stiffness, which is an important property in several applications, including for instance physical human-robot interaction. Furthermore, the many grooves on the output pulley enable multi-cable arrangements which can even further increase the transmission's stiffness. A method to ensure that the drive cables can pass smoothly between the input and output pulley was also described. Future work on this novel capstan drive will consist in testing the established model in a test bench in order to quantify the increased coefficient of friction caused by the grooves as well as to quantify the increase in drive stiffness compared to a standard capstan drive. Furthermore, the influence of the increased drive stiffness on the drive's bandwidth will be analyzed and compared to other small-ratio transmissions in order to determine if this novel drive is advantageous for physical human robot interaction.

Acknowledgements

References

[1] Roveda, L., Pedrocchi, N., Beschi, M., and Tosatti, L. M., 2018. "High-accuracy robotized industrial assembly task control schema with force overshoots avoidance". *Control Engineering Practice,* **71**, pp. 142–153.

[2] Meißner, D.-W. I. J., Schmatz, M. S. F., Beuß, D.-I. F., Sender, D.-W. I. J., Flügge, I. W., and Gorr, D.-K. F. E., 2018. "Smart human-robot-collaboration in mechanical joining processes". *Procedia Manufacturing,* **24**, pp. 264–270.

[3] Raessa, M., Sánchez, D., Wan, W., Petit, D., and Harada, K., 2019. "Teaching a robot to use electric tools with regrasp planning". *CAAI Transactions on Intelligence Technology,* **4**(1), pp. 54–63.

[4] Loughlin, C., Albu-Schäffer, A., Haddadin, S., Ott, C., Stemmer, A., Wimböck, T., and Hirzinger, G., 2007. "The dlr lightweight robot: design and control concepts for robots in human environments". *Industrial Robot: an international journal*.

[5] Xiaoqing, G., and Jidong, W., 2011. "Mechanical design and kinematic analysis of a new kind of palletizing robot". In 2011 Second International Conference on Mechanic Automation and Control Engineering, IEEE, pp. 404–408.

[6] 3d systems, 2020. Phantom premium. On the WWW, August. URL https://www.3dsystems.com/haptics-devices/3d-systems-phantom-premium.

[7] Wen, K., Harton, D., Laliberté, T., and Gosselin, C., 2019. "Kinematically redundant (6+ 3)-dof hybrid parallel robot with large orientational workspace and remotely operated gripper". In 2019 International Conference on Robotics and Automation (ICRA), IEEE, pp. 1672–1678.

[8] Wen, K., Nguyen, T. S., Harton, D., Laliberté, T., and Gosselin, C., 2020. "A backdrivable kinematically redundant (6+3)-degree-of-freedom hybrid parallel robot for intuitive sensorless physical human–robot interaction". *IEEE Transactions on Robotics*, pp. 1–17.

[9] Gosselin, F., Ferlay, F., Bouchigny, S., Mégard, C., and Taha, F., 2011. "Specification and design of a new haptic interface for maxillo facial surgery". In 2011 IEEE International Conference on Robotics and Automation, IEEE, pp. 737–744.

[10] Perret, J., and Vercruysse, P., 2014. "Advantages of mechanical backdrivability for medical applications of force control". In Workshop on Computer/Robot Assisted Surgery (CRAS).

[11] Baumann, R., and Clavel, R., 1998. "Haptic interface for virtual reality based minimally invasive surgery simulation". In Proceedings. 1998 IEEE International Conference on Robotics and Automation (Cat. No. 98CH36146), Vol. 1, IEEE, pp. 381–386.

[12] Carignan, C. R., and Cleary, K. R., 2000. "Closed-loop force control for haptic simulation of virtual environments".

[13] Baser, O., and Konukseven, E. I., 2013. "Kinematic model calibration of a 7-dof capstan-driven haptic device for pose and force control accuracy improvement". *Proceedings of the Institution of Mechanical Engineers, Part C: Journal of Mechanical Engineering Science,* **227**(6), pp. 1328–1340.

[14] Townsend, W. T., 1988. "The effect of transmission design on force-controlled manipulator performance". PhD thesis.

[15] Rooks, B., 2006. "The harmonious robot". *Industrial Robot: An International Journal,* **33**(2), pp. 125–130.

[16] Phan, S., Lioulemes, A., Lutterodt, C., Makedon, F., and Metsis, V., 2014. "Guided physical therapy through the use of the barrett wam robotic arm". In 2014 IEEE International Symposium on Haptic, Audio and Visual Environments and Games (HAVE) Proceedings, IEEE, pp. 24–28.

[17] Lu, Y., Liao, H., Hei, M., Liu, H., and Fan, D., 2015. "Development of a differential cable drive mechanism for acquiring tracking and pointing application". *Proceedings of the Institution of Mechanical Engineers, Part C: Journal of Mechanical Engineering Science,* **229**(17), pp. 3191–3200.

[18] Lu, Y., and Fan, D., 2012. "Non-intervene cable wrapping method for precise cable drive". In 2012 international conference on optoelectronics and microelectronics, IEEE, pp. 378–383.

[19] Lu, Y., and Fan, D., 2013. "Transmission backlash of precise cable drive system". *Proceedings of the Institution of Mechanical Engineers, Part C: Journal of Mechanical Engineering Science,* **227**(10), pp. 2256–2267.

[20] Xie, X., Qi, C., Zhang, L., and Fan, D., 2019. "Analytical and experimental research on transmission backlash in precise cable drive for an electro-optical targeting system". *Advances in Mechanical Engineering,* **11**(7), p. 1687814019866059.

[21] Brooks, T. L., 1990. "Telerobotic response requirements". In 1990 IEEE International Conference on Systems, Man, and Cybernetics Conference Proceedings, IEEE, pp. 113–120.

[22] Gealy, D. V., McKinley, S., Yi, B., Wu, P., Downey, P. R., Balke, G., Zhao, A., Guo, M., Thomasson, R., Sinclair, A., et al., 2019. "Quasi-direct drive for low-cost compliant robotic manipulation". In 2019 International Conference on Robotics and Automation (ICRA), IEEE, pp. 437–443.

[23] Baser, O., and Konukseven, E. I., 2010. "Theoretical and experimental determination of capstan drive slip

error". *Mechanism and Machine Theory,* **45**(6), pp. 815–827.

[24] Hymans, F., and Hellborn, A., 2013. *Der neuzeitliche Aufzug mit Treibscheibenantrieb: Charakterisierung, Theorie, Normung.* Springer-Verlag.

[25] Janovskỳ, L., 1999. *Elevator mechanical design.* Elevator World Inc.

[26] Werkmeister, J., and Slocum, A., 2007. "Theoretical and experimental determination of capstan drive stiffness". *precision Engineering,* **31**(1), pp. 55–67.

[27] Gibson, G. W. "Fred hymans and the theory of rope traction, part two".

[28] Koshak, J. W. "Traction for field personnel, part one".